



ELSEVIER

Tectonophysics 247 (1995) 49–64

TECTONOPHYSICS

# Finite-element analysis of the stress distribution around a pressurized crack in a layered elastic medium: implications for the spacing of fluid-driven joints in bedded sedimentary rock

Mark P. Fischer <sup>a,\*</sup>, Michael R. Gross <sup>b</sup>, Terry Engelder <sup>c</sup>, Roy J. Greenfield <sup>c</sup>

<sup>a</sup> *Department of Geosciences and Earth System Science Center, The Pennsylvania State University, University Park, PA 16802-7501, USA*

<sup>b</sup> *Department of Geology, Florida International University, Miami, FL 33199, USA*

<sup>c</sup> *Department of Geosciences, The Pennsylvania State University, University Park, PA 16802-7501, USA*

Received 30 May 1994; revised version accepted 21 September 1994

## Abstract

Bedding-perpendicular joints confined to individual beds in interbedded sedimentary rocks commonly exhibit spacings which are proportional to the thickness of the jointed bed, and which vary according to lithology or structural position. The mechanical explanation for this relationship is well understood when the joints are driven by far-field crack-normal tensile stresses, but poorly understood for cracks driven by elevated fluid pressures, where the crack-driving stress is the difference between the crack-normal compression and the fluid pressure in the crack. Through a series of finite-element numerical models, we investigate how various parameters influence the driving-stress distribution around pressurized cracks in layered media, and thereby identify factors influencing the spacing of fluid-driven joints. For the situation we modeled, we observe that: (1) crack-driving stress is reduced in the vicinity of pressurized joints, and that the extent of the stress reduction depends on the contrast in elastic properties between the layers; and (2) crack-driving stress distribution depends on the ambient pore pressure during jointing. These results indicate the spacing of fluid-driven joints should depend on lithology and pore pressure.

## 1. Introduction

Abundant field observations demonstrate that when bedding-perpendicular joints are confined to individual beds in a sequence of sedimentary rocks, the spacing of the joints is proportional to the thickness of the bed within which they are contained (Harris et al., 1960; Price, 1966; Mc-

Quillan, 1973; Ladeira and Price, 1981; Huang and Angelier, 1989; Narr and Suppe, 1991; Gross, 1993a). For the case when joints are driven by a far-field tensile stress, a variety of workers have shown that the correlation between joint spacing and bed thickness is a manifestation of the relationship between joint height (i.e., bed thickness) and the tensile stress distribution around an open crack (e.g., Lachenbruch, 1961; Pollard and Segall, 1987; Olson, 1993; Gross et al., in press). An open joint perturbs a homogeneous tensile stress

\* Corresponding author.

field such that local joint-normal tensile stress must be zero at the joint wall, and increases to the far-field stress at some distance from the joint. The distance from the joint to which the far-field stress is perturbed depends on the height of the joint ( $2c$ ), which in bedded sedimentary rocks is often equal to bed thickness ( $t$ ). The correlation between joint spacing and bed thickness occurs because new joints are inhibited from forming in the zone of decreased joint-normal tensile stress (i.e., stress reduction shadow of Gross et al., in press) around existing joints, and the size of the stress reduction shadow scales with joint height, which in turn corresponds to bed thickness.

Previous work on the relationship between joint spacing and bed thickness deals with cracks subjected to far-field crack-normal tensile stress<sup>1</sup> (e.g., Lachenbruch, 1961; Hobbs, 1967; Pollard and Segall, 1987; Gross et al., in press). Although absolute tensile stresses can occur under some geologic circumstances (e.g., above the neutral fiber in a buckle fold), the predominant state of stress in the brittle crust is one of triaxial compression. Under these conditions, joint propagation is believed to occur by fluid-driven jointing (e.g., Secor, 1965; Engelder and Lacazette, 1990). Although the geological literature is replete with theoretical analog, analytical and numerical analyses of joint set development in bedded rocks subjected to far-field tension (e.g., Olson, 1993; Rives et al., 1994), there is a lack of such analyses for fluid-driven joints. The principal related work appears in Pollard and Segall (1987), in which we find an analytical solution for the variation in crack-normal stress with distance  $x$  away from the center of the wall of a pressurized crack in a homogeneous, infinite elastic medium.

Fig. 1 shows the Pollard and Segall (1987) solution for cracks with internal pore pressures ( $P_p$ ) of  $-35$ ,  $-50$  and  $-70$  MPa subjected to a remote crack-normal compressive stress ( $\sigma_{xx}^r$ ) of

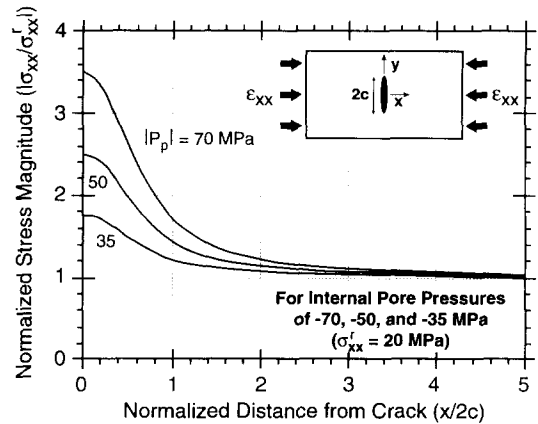


Fig. 1. Pollard and Segall (1987) analytical solution for the variation in crack-normal stress with distance  $x$  along the line  $y = 0$  away from the wall of a pressurized crack in a homogeneous, infinite elastic medium.

20 MPa<sup>2</sup>. This solution defines a zone of elevated crack-normal compressive stress in the vicinity of a dilated, pressurized crack. We suggest that the initiation of new joints is suppressed in the region of elevated joint-normal compression adjacent to dilated, pressurized joints. We further hypothesize that the spacing of pressurized joints is dependent on the lateral extent of this zone of elevated crack-normal compression. Because the width of the zone of elevated crack-normal compression scales with crack height, the spacing of fluid-driven joints confined within individual beds should also scale with the bed thickness.

To test our hypothesis, we first present finite-element numerical solutions for the two-dimensional stress distribution around a pressurized

<sup>1</sup> Throughout this paper we use the term 'crack' when discussing mode I fractures in theoretical or numerical models. We use the term 'joint' when discussing natural mode I fractures.

<sup>2</sup> Note that in their analysis, Pollard and Segall consider the case of a uniformly pressurized crack; there is no fluid in the surrounding medium. In this situation the fluid pressure imparts a compressive stress on the crack wall and they, therefore, give it a positive sign. In our analyses we assume the medium and the crack are permeated with fluid at a constant fluid pressure. Throughout this paper compressive stresses are considered positive, whereas fluid pressure is negative. We take this approach to emphasize that fluid pressure and remote compression act against one another in crack initiation.

crack confined to one layer of a layered elastic medium under far-field crack-normal compression. We present these solutions as a first-order constraint for future work on the development of fluid-driven joint sets. Following the work of Gross et al. (in press), we next examine the parameters which might influence the stress distribution around pressurized, dilated cracks, and therefore, the spacing of fluid-driven joints. Included in these parameters are the elastic properties of the local stratigraphy, unjointed bed thickness, ambient pore pressure and the fracture resistance of the beds.

## 2. Problem formulation

The natural system we are modeling is an alternating sequence of bedded sedimentary rocks containing a single pressurized joint confined to one of the stiffer layers (Fig. 2). Our models assume bedding interfaces are perfectly bonded so that there is no interbed slip. We constrain the tips of the joint to occur exactly at the layer interfaces in all our models; there is no opening of the bounding layers; and assume the joint is infinitely long in the  $z$ -direction (i.e., blade-like; Olson, 1993). For this geometry the distribution of stress around a crack is identical when viewed

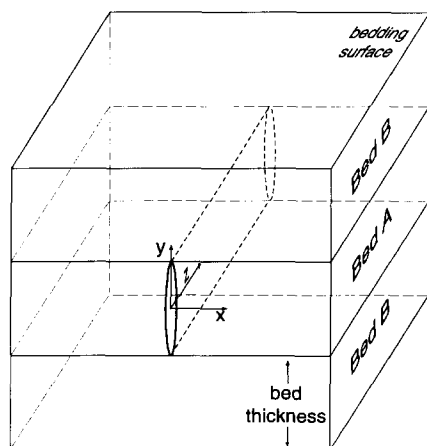


Fig. 2. Geometry of the problem investigated in this paper. In this paper the  $y$ -dimension of the crack is referred to as the height, and the  $z$ -dimension is the length.

on any  $x$ - $y$  cross section through the body. All our analyses are done on such a cross section. In modeling this situation, we do not suggest fluid-driven joints initiate first in rocks with high relative Young's moduli, as is the case for joints driven by far-field tension (e.g., Hobbs, 1967; Gross et al., in press). We use the case of a crack confined to a stiffer lithology only as one possible reference state. Recent work by Apotria et al. (1994) and Fischer (1994) analyzes the parameters controlling the initiation and stratigraphic distribution of fluid-driven joints.

We utilize linear elastic fracture mechanics (LEFM; Broek, 1986) to describe the stress and displacement distributions in the vicinity of the crack. This approach results in a large elastic stress concentration at the tips of the crack in our analyses; in some cases large enough to suggest the crack should propagate across the bedding interface and into the bounding beds. This stress concentration is a purely elastic phenomenon, unlikely to occur in rocks because high stresses at the tips of joints are most likely relieved by localized inelastic deformation or bedding slip (e.g., Achenbach et al., 1979; Keer and Chen, 1981; Watkins, 1992). The presence of crack-tip stress concentrations in our models primarily affects the distribution of stress in the vicinity of the crack tip, particularly in the uncracked layers adjacent to a crack tip (e.g., Helgeson and Aydin, 1991); the stress distribution in the cracked layers is not significantly influenced. For completeness, we describe the perturbation of stress in the uncracked layers related to the crack tip stress concentration, but emphasize that these stress distributions only occur in ideal, linear elastic materials with perfectly bonded interfaces.

### 2.1. Fluid-driven jointing

The process of fluid-driven jointing is governed by a balance of forces which act to open or close a crack. Crack opening is induced by pore pressure ( $P_p$ ) within a crack whereas crack closure occurs under a compressive remote stress ( $\sigma^r$ ). Stress perturbations occur near fluid-filled cracks in compressive stress fields over a range of

fluid pressures, and are caused by the difference between fluid pressure at a crack wall and the remote compressive stress. Until the fluid pressure in a crack exceeds the remote stress, the crack will remain closed and there is no stress perturbation. The instant the magnitude of the fluid pressure exceeds  $\sigma_{xx}^r$ , however, the crack dilates and the ambient stress field is perturbed, such that the local  $\sigma_{xx} > \sigma_{xx}^r$ . In the absence of subcritical crack growth (e.g., Atkinson and Meredith, 1987a), a pressurized, dilated crack is stable (i.e., it will not extend) as long as the mode I stress intensity ( $K_I$ ; Broek, 1986) at the tip of the crack does not exceed the fracture toughness ( $K_{Ic}$ ; Atkinson and Meredith, 1987b) of the material at the crack tip.

Because field data from a variety of sedimentary basins indicates horizontal stress magnitude is directly related to ambient pore pressure (e.g., Salz, 1977; Breckels and van Eekelen, 1982; Bell, 1990; Teufel et al., 1991; Gaarenstroom et al., 1993), Fischer and Engelder (1994) noted that poroelastic increases in horizontal stress must be accounted for in any analysis of fluid-driven jointing. However, an investigation of jointing in poroelastic, interbedded sedimentary rocks is beyond the scope of this paper. As a first step in understanding the development of fluid-driven joint sets, we instead consider only a static, non-poroelastic case: fluid-driven joints are discussed only in terms of the fluid pressure and crack-normal remote stress acting on the wall of a stable

(i.e., non-propagating) crack. The details of poroelasticity and the initiation of fluid-driven joints are discussed in Engelder and Lacazette (1990), Kümpel (1991), Fischer (1994) and Engelder and Fischer (1994).

### 3. Numerical modeling procedure

Finite-element numerical modeling in this study was accomplished using the interactive finite-element program FRANC (FRacture ANalysis Code; Wawrzynek and Ingraffea, 1987) developed at Cornell University. FRANC simulates the familiar  $r^{-1/2}$  singularity in the elastic crack-tip stress field, where  $r$  is the radial distance away from the crack tip (e.g., Lawn and Wilshaw, 1975; Broek, 1986), by surrounding the tips of each crack with a rosette of eight quadratic, triangular, isoparametric, quarter-point elements (Barsoum, 1976). Other portions of any mesh are comprised of eight-noded quadrilateral or six-noded triangular, quadratic, isoparametric elements. The accuracy of FRANC has been proven in numerous applications (e.g., Linsbauer et al., 1989; Ingraffea, 1990; Bittencourt et al., 1992).

Fig. 3 depicts the finite-element mesh utilized throughout most of this study, and the boundary conditions we employed in all our models. For our primary model, we discretized a 4-m-long by 2-m-high rectangular region and divided the region into three layers. The middle jointing layer

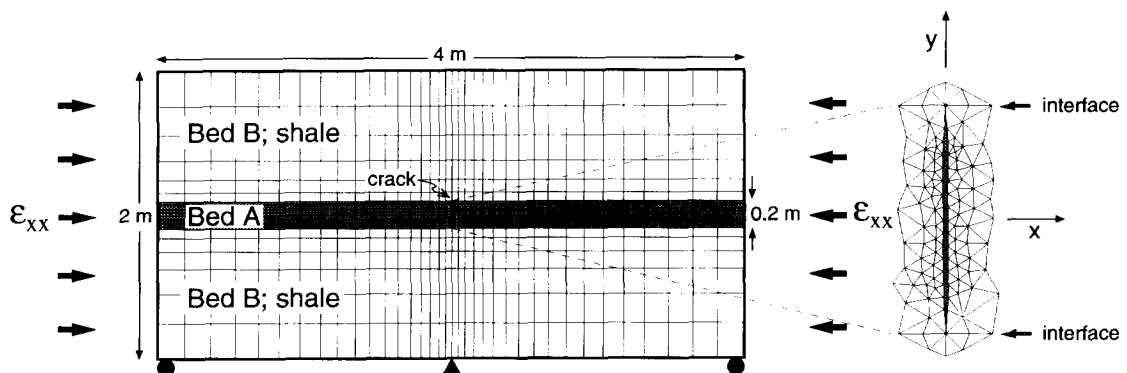


Fig. 3. Finite-element mesh and boundary conditions utilized in portions of this study. The mesh is identical to that utilized by Gross et al. (in press).

Table 1

Model material properties used in this study. Values are representative of numerous published values as compiled from various sources (e.g., Blair, 1955, 1956; Birch, 1966; Hatheway and Kiersch, 1982; Senseny and Pfeifle, 1984; Atkinson and Meredith, 1987a) and reported in Fischer (1994).

Material property	Dolostone	Shale
Fracture toughness, $K_{Ic}$ (MPa · m <sup>1/2</sup> )	1.7	0.9
Poisson ratio, $\nu$	0.26	0.14
Shear modulus, $G$ (GPa)	22	7
Young's modulus, $E$ (GPa)	56	16

(bed A) is given different elastic properties for various individual models, whereas we assigned the elastic properties of shale (Table 1) to the bounding, unjointed layers (beds B) for all our models. In all models the mesh is constrained to displace only in the  $x$ -direction along the bottom edge, and is fixed in both  $x$  and  $y$  at the midpoint of the bottom edge. The top of each model is free to move according to the deformations of the mesh, but is not a stress-free surface. To simulate far-field crack-normal compressive stress, we apply a constant contractional longitudinal strain ( $\epsilon_{xx}$ ) to the entire model prior to the introduction of a crack. After the application of a constant strain, we introduce a crack to the center of the mesh using FRANC's automatic crack growth and remeshing algorithms. Remeshing is done so that discretization in regions near the new crack is much finer than the remainder of the model mesh (see inset in Fig. 3). After a new, cracked model mesh is generated, the crack is loaded with a uniform internal pressure. Our model is sufficiently large so that edge effects (i.e., inaccuracies in the numerical results which inherently occur near the edges of discretized regions of finite size) do not influence the numerical solution in the region near the crack.

We present results from eight different models: one model designed to investigate the theoretical stresses and displacements in an interbedded dolostone and shale sequence, three models designed to determine the effects of contrasting layer elastic moduli on the stress perturbation around a crack, and four models designed to assess the impact of the relative thicknesses of

cracked and bounding beds on the stress perturbation around a crack. The first four models utilize the mesh depicted in Fig. 3, whereas the other four models required uniquely designed meshes we describe later.

## 4. Model results

### 4.1. Dolostone and shale model

In this model bounding bed elastic properties are those of shale and the cracked bed is assigned the elastic properties of dolostone (Table 1). Uniform longitudinal contractional strain ( $\epsilon_{xx}$ ) of  $3.571 \times 10^{-4}$  was applied to this model prior to the introduction of a crack. The theoretical crack-normal stress ( $\sigma_{xx}^r$ ) resulting from this strain is 20 MPa in the dolostone and 5.71 MPa in the shale. Edge effects in the model resulted in a slight longitudinal variation in  $\sigma_{xx}$ , where in each bed the average difference between  $\sigma_{xx}$  calculated at any  $x$ -position in the model and the theoretical value of  $\sigma_{xx}^r$  was less than 3.0% of the theoretical  $\sigma_{xx}^r$ . The mean  $\sigma_{xx}$  is 20.5 MPa in the dolostone, and 5.66 MPa in the bounding shale beds for this model. These values of  $\sigma_{xx}$  are equivalent to the remote crack-normal compressive stress ( $\sigma_{xx}^r$ ) in the model. A uniform pore pressure of  $-35$  MPa was applied to the walls of the crack in this model. This combination of crack-normal compression and internal fluid pressure results in a 15-MPa tensile effective stress at the crack wall.

#### *Perturbation of $\sigma_{xx}$ upon pressurization of the crack*

The two-dimensional distribution of crack-normal stress ( $\sigma_{xx}$ ) throughout a portion of the right half of the dolostone and shale model is depicted in Fig. 4. In the dolostone, crack-normal stress reaches a maximum value equal to  $P_p$  at the wall of the crack, and decreases to  $\sigma_{xx}^r$  with distance  $x$  away from the crack. In the shale layers,  $\sigma_{xx}$  decreases close to the crack tips and increases to the far-field value away from the crack (Fig. 4). Steep stress gradients occur across the layer interfaces. Near each end of the crack  $\sigma_{xx}$  de-

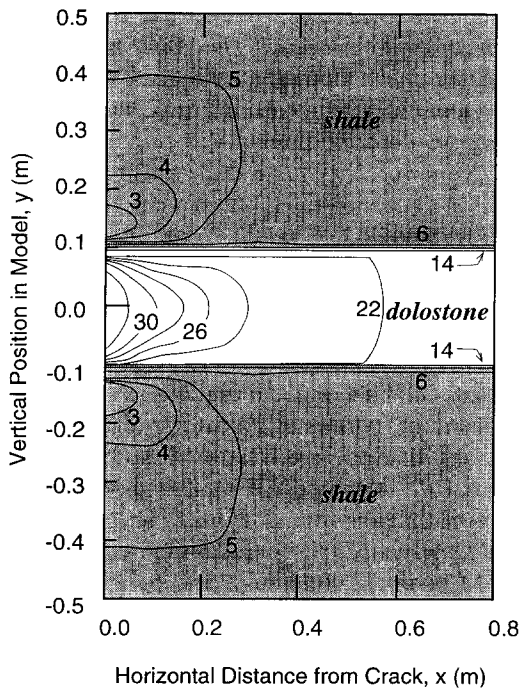


Fig. 4. Contours of crack-normal stress ( $\sigma_{xx}$ ) in the dolostone and shale model. See Table 1 for model material properties. Applied strain,  $\epsilon_{xx} = 3.571 \times 10^{-4}$ . Contours in MPa, and unless labeled, contour interval is 2 MPa.

creases due to the stress concentrating effect of the sharp crack tip. The reduction in stress near the crack tips occurs because tensile (i.e., negative) crack-tip stresses counteract the far-field compressive stress, resulting in the decrease in compressive stress magnitude near the crack tips. The tensile crack-tip stress concentrations perturb the local compressive stress field in the shale layers for distances up to  $\sim 0.4$  m from the crack (Fig. 4). Beyond  $\sim 0.4$  m from the crack, the stress in the shale beds is the same as the prepressurization stress.

The shape of stress contours in the dolostone beds is concave towards the crack because the crack opens with an elliptical profile, and therefore, the greatest amount of elastic strain occurs by crack opening along the middle of the dolostone bed. Consequently, the perturbation in  $\sigma_{xx}$  caused by fluid in the crack is greatest and extends farthest along the center of the dolostone bed.

### Bedding-parallel displacements

The two-dimensional distribution of bedding-parallel displacements ( $u$ ) that developed in the model is shown in Fig. 5. After formation of a crack in the middle bed, longitudinal elastic displacements throughout the model are not constant, and the shape of displacement profiles taken vertically through the model varies dramatically with distance from the crack. Near the crack, the elliptical profile of the dilated model joint is reflected in the distinct concave-inward curvature of the displacement profile in the dolostone bed, and results in a steep displacement gradient between the center of the cracked bed and the bedding interface. With increasing horizontal distance from the crack, this steep displacement gradient shallows and extends further into the shale beds. At horizontal distances greater than  $\sim 0.8$  m, the influence of the crack on the bedding-parallel displacement is greatly reduced, and the displacement profiles are nearly straight.

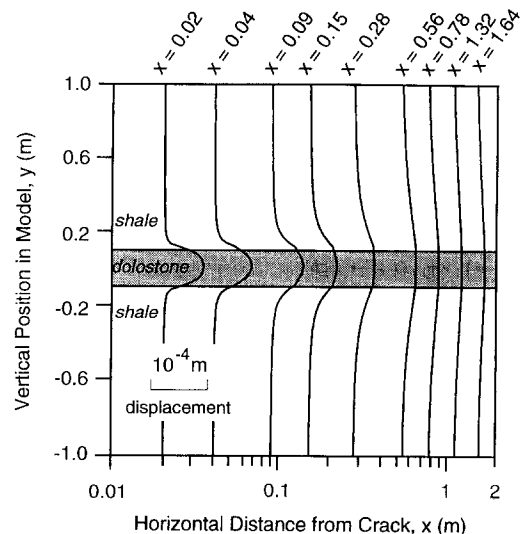


Fig. 5. Vertical displacement profiles (i.e., loose lines) taken at different  $x$ -positions through the right half of the dolostone and shale model. Displacement of each line is measured relative to an originally straight, vertical line. A straight line means there is uniform  $x$ -displacement throughout the model at the position of the profile. Displacement along each profile is measured with the inset scale.

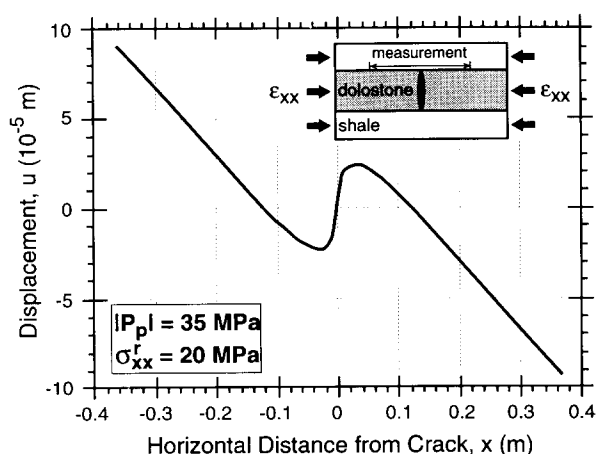


Fig. 6. Longitudinal displacement along the interfaces of the dolostone and shale model resulting from a superposition of uniform longitudinal contraction,  $\epsilon_{xx} = 3.571 \times 10^{-4}$  and uniform fluid pressure,  $P_p = -35$  MPa. Displacement of each point is measured relative to the original position. Negative displacements occur when material is displaced in the negative  $x$ -direction. To the left of the crack, negative displacements occur when material moves away from the crack. To the right of the crack, negative displacements result when material moves closer to the crack.

The horizontal variation in displacement that developed along the bedding interface of our model is shown in Fig. 6. Longitudinal displacement along the interfaces is symmetric about the crack and zero exactly at the crack tip (i.e.,  $x = 0$ ,  $y = \pm 0.1$ ). Near the crack, dilation due to fluid pressure in the crack results in displacement of material away from the crack. However, these outward displacements occur only near the crack, and after increasing linearly to a distance of  $\sim x = 0.02$  m, they decay in a non-linear manner to a distance of  $\sim 0.1$  m from the crack. At  $x$ -distances greater than  $\sim 0.1$  m from the crack, longitudinal displacement along the interface is not influenced by the crack, and total displacement varies linearly with increasing distance away from the crack (i.e., constant strain).

#### Bedding-parallel shear stress

Fig. 7 depicts the two-dimensional variation in bedding-parallel shear stress ( $\tau_{xy}$ ) along several vertical profiles through the model. Shear stress is zero along the center of the dolostone bed and

throughout the model at vertical ( $y$ ) distances greater than  $\sim 0.5$  m from the bedding interfaces. Close to the crack  $\tau_{xy}$  is maximum at the interface and decreases rapidly to zero away from the interface. However, with increasing horizontal distance from the crack, the maximum  $\tau_{xy}$  occurs slightly above the interface and bedding-parallel shear stresses are developed in the shale beds at greater distances from the bedding interfaces. Along the interface,  $\tau_{xy}$  increases to a maximum near the crack and decreases to a negligible value at  $\sim 1.0$  m from the crack (Fig. 8).

#### 4.2. Effects of contrasting elastic moduli

Hobbs (1967) demonstrated that the  $x$ -distance to which  $\sigma_{xx}$  was perturbed around an open joint depends not only on crack height, but also on the ratio of the cracked bed Young's modulus ( $E_A$ ) to bounding bed shear modulus ( $G_B$ ). His result suggests that in addition to joint height (i.e., bed thickness), the spacing of joints formed in response to far-field joint-normal tension is also dependent on the elastic properties of the involved stratigraphy. Although Narr and Suppe (1991) question the influence of stratigraphy on joint spacing, field data presented by Gross (1993b) exhibit a variation in joint spacing with lithology. Results of numerical modeling by Gross et al. (in press) likewise confirm Hobbs' analytical results, but suggest the extent to which  $\sigma_{xx}$  is perturbed around an open crack is not as strongly dependent on  $E_A/G_B$  as suggested by Hobbs (1967).

To examine the effects of contrasting elastic moduli on the  $\sigma_{xx}$  distribution around pressurized cracks in layered media, we use the finite-element mesh depicted in Fig. 3, and apply a uniform longitudinal contractional strain to each of three models prior to pressurization of the crack. The bounding bed elastic properties are those of shale, cracked bed Poisson ratio is 0.25, and the Young's modulus of the cracked bed is 17.5, 35 and 70 GPa, in each of the three successive models. After contracting a model by  $2.857 \times 10^{-4} \epsilon_{xx}$ , we pressurize the crack to a uniform  $P_p$  that is 3 MPa above  $\sigma_{xx}^r$  in the cracked bed

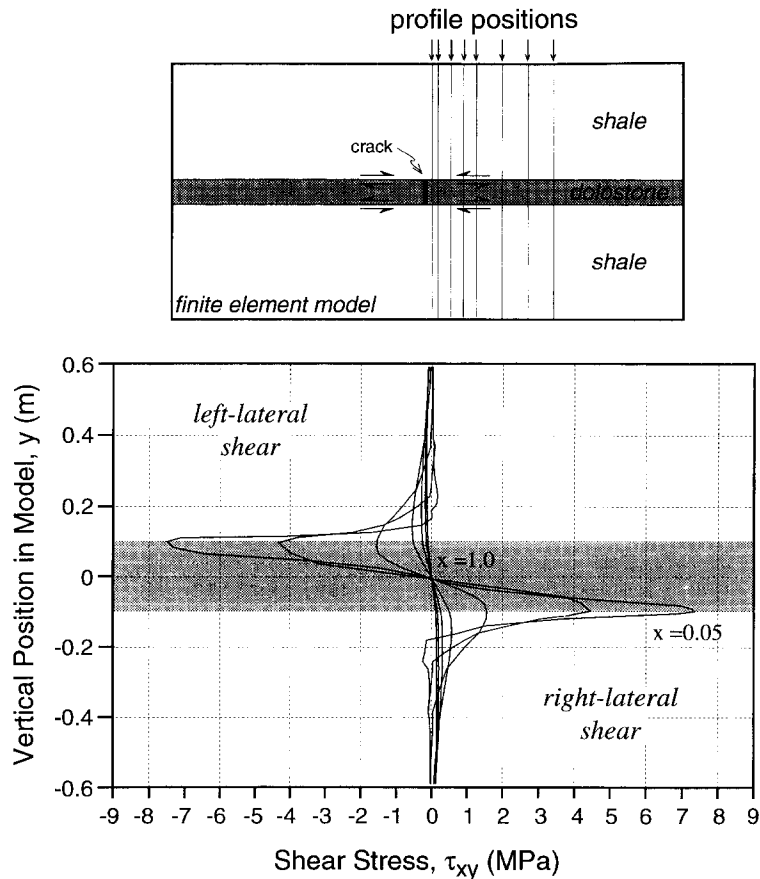


Fig. 7. Variation in bedding-parallel shear stress ( $\tau_{xy}$ ) along several vertical profiles through the right half of the dolostone and shale model. Profiles taken at  $x$ -positions of 0.05, 0.1, 0.2, 0.3, 0.4, 0.6, 0.8, and 1.0 m. Note that left-lateral shear is negative and right-lateral shear is positive. Shear stress distribution is symmetric about both the vertical and horizontal axes of the model such that left-lateral shear occurs in the upper right and lower left quadrants of the model, and right-lateral shear occurs in the upper left and lower right quadrants.

(i.e., the pre-pressurization  $\sigma_{xx}$ ). By designing our models in this fashion, we implicitly assume that each bed cracks at a constant value of  $(P_p - \sigma_{xx}^r)$ . This is not likely in reality, but we defer discussion of the actual behavior until later, presently analyzing only the simple case. Although edge effects resulted in a longitudinal variation in  $\sigma_{xx}$  in each model, the average difference between the theoretical  $\sigma_{xx}^r$  and the numerically calculated  $\sigma_{xx}$  at any position in the middle bed of each model is less than 2.0%. We use the numerically determined average  $\sigma_{xx}$  value in the middle bed to normalize the results presented below (i.e.,  $\sigma_{xx}^{\text{avg}} = \sigma_{xx}^r$ ). To eliminate the influence of

crack height on the size of the perturbed zone around a crack, we also normalize horizontal distances by the cracked bed thickness ( $t_A$ ).

Fig. 9 depicts contours of normalized crack-normal compressive stress ( $\sigma_{xx}/\sigma_{xx}^r$ ) throughout the jointed bed of the three models we conducted. This figure reveals that under these specific model conditions, the zone of increased crack-normal compression adjacent to a pressurized, dilated crack (i.e., pore pressure shadow of Fischer, 1994), decreases in width with increasing Young's modulus of the cracked bed ( $E_A$ ). If the spacing of fluid-driven joints is influenced by the width of the pore pressure shadow around exist-

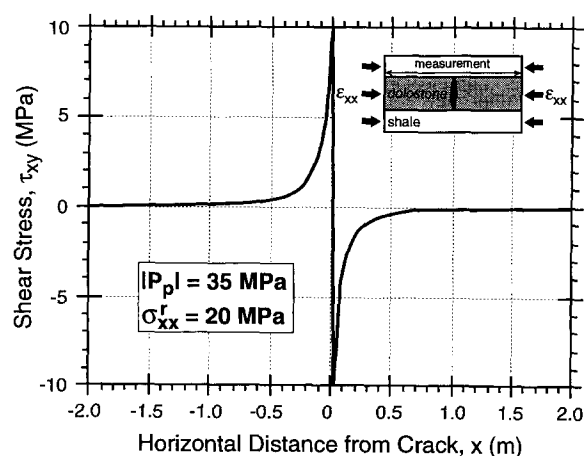


Fig. 8. Variation in bed-parallel shear stress along the interface of the model after pressurization of the crack. Shear stress sign convention is the same as in Fig. 7. Note that the maximum shear stress attained in any model is a function of the contrast in elastic moduli between beds A and B, the fluid pressure in the crack and the remote compressive stress.

ing dilated joints, this result suggests that for beds of equal thickness, fluid-driven joint spacing should also depend on lithology. This result is in agreement with numerical solutions and field data presented by Gross et al. (in press).

#### Crack-driving stress

Although Fig. 9 illustrates that the mechanical properties of beds affect the distribution of crack-normal compressive stress around a pressurized crack, a clear understanding of how lithology influences joint spacing requires information on how stress perturbations around pressurized cracks might influence the initiation of nearby cracks. For pressurized cracks in compressive stress fields, the parameter controlling crack initiation is the crack-driving stress ( $\Delta\sigma$ ), and was defined by Pollard and Segall (1987) as:

$$\Delta\sigma = |\sigma_{xx}^c| - \sigma_{xx}^r \quad (1)$$

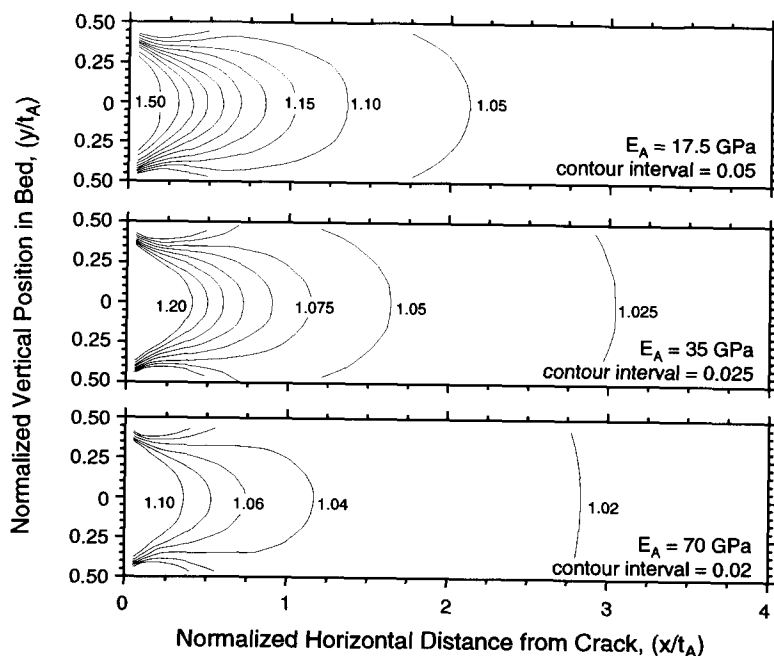


Fig. 9. Contours of normalized-crack normal stress ( $\sigma_{xx}/\sigma_{xx}^r$ ) in the cracked bed of three different models after pressurization of a crack. Contours are in units of remote crack-normal stress (i.e.,  $n \cdot \sigma_{xx}^r$ , where  $n$  is the contour value). Remote stresses are 5, 10 and 20 MPa and pore pressures are approximately 8, 13 and 23 MPa respectively, for the  $E = 17.5, 35$  and  $70$  GPa models.

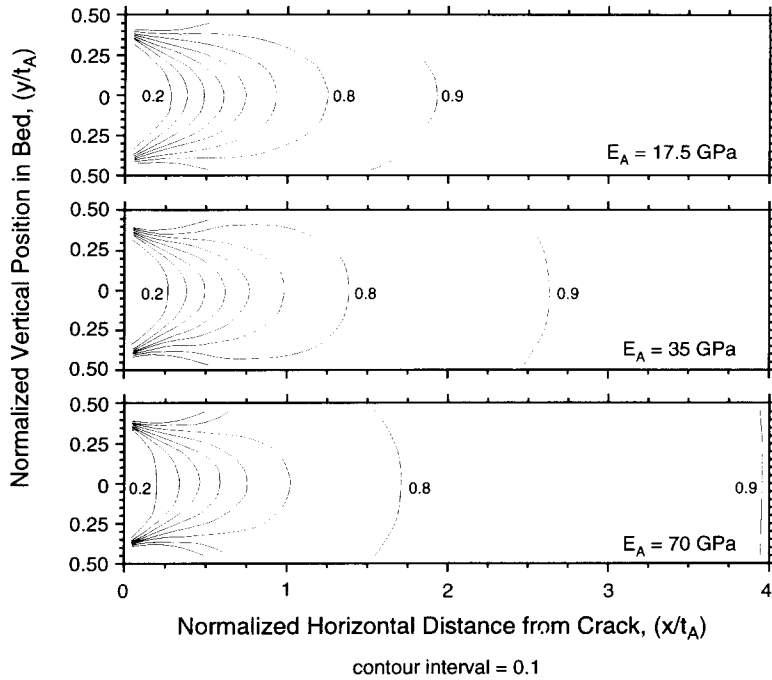


Fig. 10. Contours of normalized crack-driving stress ( $\Delta\sigma/\Delta\sigma_{\max}$ ) in the jointed bed of three different models after formation of a crack. Maximum driving stress ( $\Delta\sigma_{\max}$ ) is 3 MPa in each model.

where  $\sigma_{xx}^c$  is the normal stress acting on a crack wall and  $\sigma_{xx}^r$  is the remote crack-normal stress<sup>3</sup>. For the situation we are modeling,  $\sigma_{xx}^c = P_p$  and  $\sigma_{xx}^r$  is equal to the bedding-parallel compressive stress prior to pressurization of the crack in each model. Note that Eq. 1 defines the maximum driving stress in a model ( $\Delta\sigma_{\max}$ ), where  $\sigma_{xx}^r$  is a constant. After dilation of the crack, local crack-driving stress is given by:

$$\Delta\sigma = |\sigma_{xx}^c| - \sigma_{xx} \quad (2)$$

where  $\sigma_{xx}$  is a function of  $x$  and  $y$ . Because  $\sigma_{xx}$  varies throughout the cracked bed after pressurization of the crack, local crack-driving stress likewise varies. It is this spatial variation in crack-driving stress which influences the initia-

tion of new cracks in the vicinity of existing dilated cracks. This analysis applies to poroelastically-induced changes in  $\sigma_{xx}^r$  as long as it is understood that the stress perturbation depends on  $\Delta\sigma$  and not  $\sigma_{xx}^r$ .

Fig. 10 depicts contours of normalized crack-driving stress in the cracked bed of the three models shown in Fig. 9. To determine the two-dimensional distribution of driving stress, we assume the model is permeated with fluid at a uniform  $P_p$ , and use Eq. 2 to calculate  $\Delta\sigma$  throughout the model where  $\sigma_{xx}$  is a function of  $x$  and  $y$  as shown in Fig. 9. The maximum driving stress in each model ( $\Delta\sigma_{\max}$ ) is the difference between the fluid pressure in the crack, and the pre-pressurization  $\sigma_{xx}$  in the center bed of a given model (i.e.,  $\sigma_{xx}^r$ ). For each plot, the driving stress is normalized by  $\Delta\sigma_{\max}$  in the model, which was arbitrarily set at 3 MPa for all cases.

It is seen from Fig. 10 that crack-driving stress is zero at the wall of the crack, and increases to  $\Delta\sigma_{\max}$  with increasing  $x$ -distance from the crack. Under our specific model conditions, the width of

<sup>3</sup> Note that Pollard and Segall (1987) denote pore pressure as a positive quantity, and therefore do not utilize the absolute value of  $\sigma_{xx}^c$ . Use of the absolute value of  $\sigma_{xx}^c$  is necessitated by our designation of pore pressure as a negative quantity.

the zone of decreased driving stress (i.e., driving stress shadow of Fischer, 1994) is greater in beds with larger relative Young’s moduli. This suggests that pressurized joints in stiffer (i.e., high relative  $E$ ) lithologies can interact with one another over wider distances than joints in less stiff lithologies. Previous work by Hobbs (1967) and Gross et al. (in press) established the same relationship between  $E_A$  and the driving-stress shadow around cracks in layered elastic media subjected to remote crack-normal tensile stress.

4.3. Pore pressure effects

It is evident from Fig. 1 that for a given  $\sigma^r$ , the magnitude of normalized crack-normal stress at any  $x$ -position in the model should depend on  $P_p$ . The distribution of crack-driving stress around a pressurized crack is likewise dependent on the fluid pressure in the crack. If the spacing of fluid-driven joints is related to the lateral extent of a local driving-stress shadow, then the dependence of shadow width on  $P_p$  suggests the spacing of fluid-driven joints may also be related to the ambient  $P_p$  during joint initiation.

Fig. 11 depicts the variation in crack-driving stress with distance  $x$  away from the center of a pressurized crack in the middle bed of a model where the bounding beds are shale and the middle bed is dolostone (Table 1). Longitudinal con-

tractional strain is applied to the model, resulting in a remote crack-normal compressive stress of 10 MPa in the dolostone bed. The graphs show the lateral variation in crack-driving stress away from the wall of a crack pressurized to  $-35$ ,  $-50$  and  $-70$  MPa. It is seen from Fig. 11 that the  $x$ -distance at which a given crack-driving stress is first exceeded depends on the pore pressure in the crack. For any specific set of material properties, a given crack-driving stress is achieved at closer  $x$ -distances at higher pore pressures. In other words, the width of the driving-stress shadow around a pressurized crack decreases with increasing pore pressure.

4.4. Effects of bounding bed thickness

Ladeira and Price (1981) suggested the spacing of joints in competent beds is affected by the thickness of adjacent incompetent beds. From field data collected in Carboniferous flysch exposed near Devon and Cornwall, U.K., they argue that for jointed beds of equal thickness, joints are more closely spaced when the thickness of unjointed shale layers bounding the jointed beds decreases (Fig. 12). This effect becomes more pronounced when the ratio of adjacent unjointed

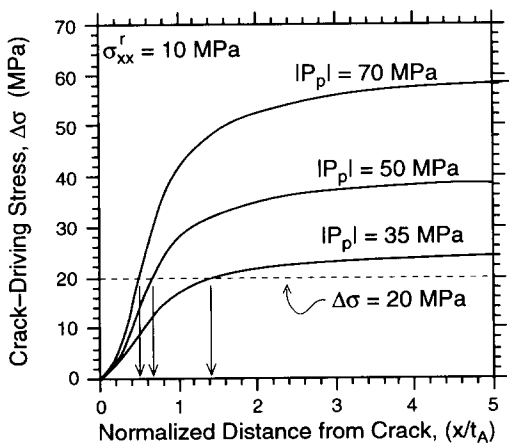


Fig. 11. Variation in crack-driving stress with distance  $x$  away from the wall of a pressurized crack. Compare  $x$  distance at which 20 MPa of driving stress is first achieved.

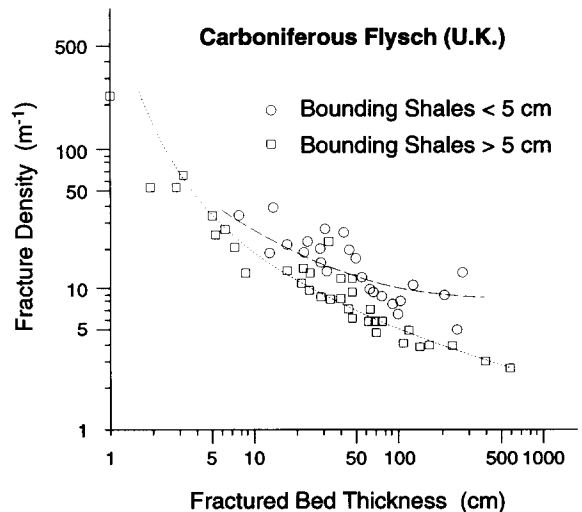


Fig. 12. Data of Ladeira and Price (1981) demonstrating a variation in fracture density as a function of the thickness of bounding, unfractured shale beds. Fracture density is defined as the number of fractures per meter of bed length.

bed thickness to jointed bed thickness ( $t_B/t_A$ ) decreases.

To test the influence of bounding bed thickness ( $t_B$ ) on the potential spacing of fluid-driven joints, we examined the variation in  $\Delta\sigma$  around a crack for four ratios of  $t_B/t_A$ . The four different finite-element meshes utilized in this analysis exhibit  $t_B/t_A$  ratios of 0.66, 0.33, 0.2 and 0.1, and are shown in Fig. 13. Each of these models consists of several alternating weak (low relative  $E$ ) and strong layers. Thinner weak beds are assigned the elastic properties of shale (Table 1),

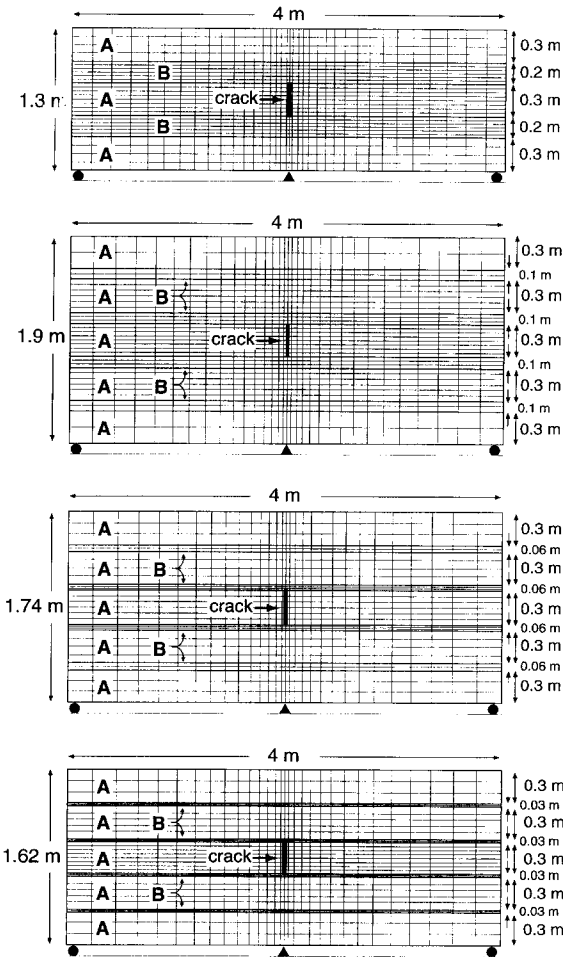


Fig. 13. Finite-element meshes utilized in testing the influence of unfractured, bounding bed thickness on the stress distribution in a cracked bed. Detail of mesh around crack omitted. Meshes all comprised of quadratic, six-noded triangular and eight-noded quadrilateral isoparametric elements.

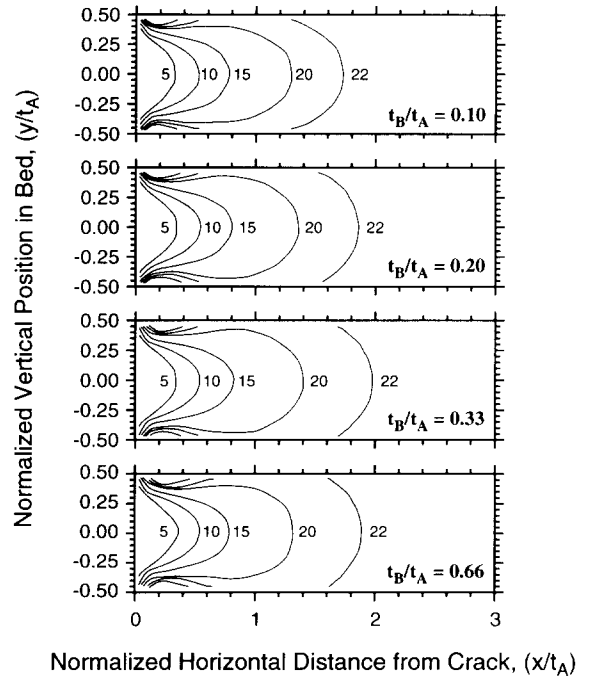


Fig. 14. Contours of crack-driving stress ( $\Delta\sigma$ ) in the cracked bed of four models, each with different ratios of uncracked bed thickness ( $t_B$ ) to cracked bed thickness ( $t_A$ ).

whereas in the other beds:  $E = 35$  GPa and  $\nu = 0.25$ . The models are first subjected to a contractional longitudinal strain ( $\epsilon_{xx}$ ) of  $2.857 \times 10^{-4}$ . After application of compressional strain, a crack in the stiff layer is pressurized with a uniform pressure of  $-35$  MPa.

Fig. 14 depicts contours of crack-driving stress in the cracked bed of each of the four models. It is readily apparent from this figure that for the  $t_B/t_A$  ratios examined, there is no clear relationship between the lateral extent of a driving-stress shadow adjacent to a pressurized crack and the thickness of adjacent uncracked beds. When compared at the 22-MPa  $\Delta\sigma$  contour, driving-stress shadow widths are not dramatically different, and appear to first increase with increasing  $t_B/t_A$ , but then to decrease with increasing  $t_B/t_A$ . Because the observed variations are slight and nonsystematic, we attribute them primarily to inaccuracies in the numerical solution and the contouring algorithm. Consequently, we conclude that when beds are bonded together, the thickness of un-

fractured beds adjacent to a cracked layer does not significantly influence the distribution of driving stress in the cracked layer.

Another conclusion we draw from our numerical results is that in regions where there is a variation in joint spacing as a function of bounding bed thickness (Fig. 12), the boundary conditions employed in our models may not apply. As testament to this we note that Ladeira and Price (1981) qualitatively attribute the variation in joint density with bounding bed thickness they observed to differences in cohesion at the bedding interfaces, implying interbed slip. Because all our models assume perfectly bonded interfaces, we cannot resolve affects associated with interbed slip. Our results suggest future investigations of Ladeira and Price's proposed relation between bounding bed thickness and joint density should be conducted using models incorporating interbed slip.

## 5. Discussion: fluid-driven joint spacing

Previous work on joint spacing demonstrates that both the positively skewed spacing distribution (e.g., Huang and Angelier, 1989), and the correlation between bed thickness and median joint spacing (e.g., Narr and Suppe, 1991; Gross, 1993a) commonly observed in bedded sedimentary rocks result from mechanical crack interactions during joint set development (e.g., Rives et al., 1992). Cracks interact with one another because of the local  $\Delta\sigma$  reduction near a crack. New cracks are inhibited from forming in these regions of reduced  $\Delta\sigma$ . As noted by Narr and Suppe (1991), Gross et al. (in press) and Fischer (1994), the initiation of new cracks is controlled by the distribution of  $\Delta\sigma$ , as well as the distribution of flaws and flaw sizes in the rocks. This relationship serves to enhance the influence of lithology on joint spacing.

Field observations of joint surface morphology indicate that joints initiate from a single point, often a concretion, bedform, fossil fragment or other flaw in the rock (e.g., Engelder, 1987). Through the equation:

$$\sigma_f = \{K_{lc}\} \{Y \sqrt{\pi c}\} \quad (3)$$

linear elastic fracture mechanics (e.g., Broek, 1986) relates the stress necessary to initiate a macroscopic joint ( $\sigma_f$ ; fracture stress), to the size ( $c$ ) and shape ( $Y$ ) of an initial flaw, as well as intrinsic rock strength ( $K_{lc}$ ; fracture toughness; Atkinson and Meredith, 1987b). A flaw will propagate and grow into a macroscopic joint when the crack-driving stress ( $\Delta\sigma$ ) equals the fracture stress ( $\sigma_f$ ) for that given flaw.

The range of flaw sizes present in rocks results in a spatially inhomogeneous fracture stress, where rock strength depends not only on the size, but also on the location of flaws in the rock. As noted by Gross et al. (in press), for a given flaw size, stiffer (i.e., larger relative  $E$ ) lithologies generally exhibit larger fracture toughnesses and, therefore, require larger fracture stresses. From a review of published  $K_{lc}$  values, it is evident that for penny-shaped flaws with a 3-cm diameter ( $c =$  radius of penny;  $Y = 1.77$  in Eq. 3), fracture stresses in shale ( $E \sim 16$  GPa; Table 1) are  $\sim 2$  MPa, whereas in carbonates ( $E \sim 56$  GPa; Table 1)  $\sigma_f \sim 4$  MPa. This dependence of fracture stress on Young's modulus is significant because it magnifies the influence of elastic properties on the driving-stress shadow around a pressurized crack, enhancing the influence of lithology on joint spacing.

Fig. 15 is a plot of crack-driving stress along the line  $y = 0$  for the three models shown in Fig. 10. If the fracture stress of the beds were independent of  $E_A$ , and therefore equal, driving-stress shadow width (i.e., the normalized horizontal distance at which  $\Delta\sigma = \sigma_f$ ) is an increasing function of  $E_A$ . However, because fracture stresses are known to increase with increasing Young's modulus, the effect of lithology on driving-stress shadow width, and therefore joint spacing, is significantly magnified. To illustrate this effect, compare the difference in driving-stress shadow widths shown by the thin arrows in Fig. 15 with that obtained by assuming  $\sigma_f = 2.0$ , a value independent of  $E_A$  (the thick arrow in Fig. 15). For a constant  $\sigma_f = 2.0$ , driving stress shadow width is roughly 1.0 times the bed thickness (i.e.,  $x/t_A$ ) in all models, with slightly larger shadow widths obtained in stiffer lithologies. When  $\sigma_f$  increases with increasing  $E_A$ , however, the dependence of

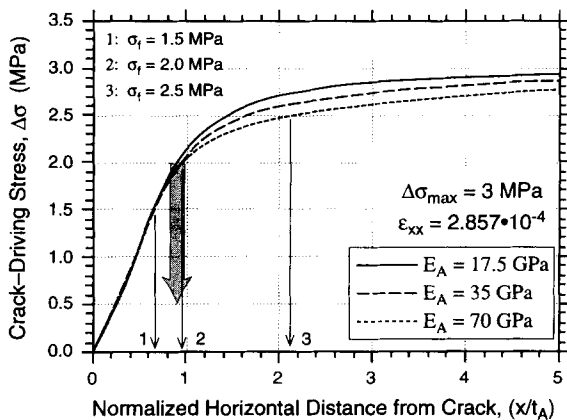


Fig. 15. Variation in crack-driving stress with distance  $x$  away from the center of the wall of a pressurized crack in three models where the Young's modulus of the cracked bed is varied. Thick arrow shows driving-stress shadow width for the case when  $\sigma_f$  does not vary with  $E_A$ . Thin arrows show horizontal extent of driving-stress shadow for the case when  $\sigma_f$  increases with increasing  $E_A$ . For the latter case,  $\sigma_f$  is respectively assumed to be 1.5, 2.0 and 2.5 MPa in the models with  $E_A = 17.5, 35$  and  $70$  GPa. This variation in fracture stress variation is arbitrary, but of the same order of magnitude expected for the modeled range of Young's moduli.

driving-stress shadow width on  $E_A$  is greatly enhanced. Because there is a natural tendency for stiffer lithologies to exhibit greater fracture stresses (e.g., Gross et al., in press), the spacing of fluid-driven joints should be even more strongly dependent on lithology than suggested by Fig. 10.

## 6. Conclusions

Our numerical models of the stress and displacement distributions around a pressurized crack in layered elastic medium provide a first-order constraint for future work on the spacing of fluid-driven joints. In complex systems such as these, there is a tendency for oversimplification of model boundary or initial conditions. In modeling a larger portion of the natural system, and by not explicitly prescribing stresses and displacements in the vicinity of the joint or along layer interfaces, we hope to have avoided many such oversimplifications. Our numerical results should be considered by other workers when designing boundary and initial conditions in similar models with reduced degrees of freedom.

The development of joint sets is largely controlled by the mechanical interaction of cracks. Crack interaction occurs because joints locally perturb far-field stresses and influence the initiation of new joints in the vicinity. We characterize the distribution of crack-normal stress around a dilated, pressurized crack confined to one layer of a layered elastic medium and demonstrate that in the vicinity of the crack: (1) crack-normal compressive stress is increased; (2) large shear stresses develop along bedding interfaces; and (3) crack-driving stress is reduced.

The extent to which crack-driving stress is reduced in the vicinity of the crack is dependent on the elastic properties of the involved stratigraphy and the pore pressure in the crack. Because joint spacing depends on the distribution of crack-driving stress, our simple effective stress analysis predicts the spacing of fluid-driven joints should depend on lithology and ambient pore pressure during jointing. The dependence of fracture stress on Young's modulus enhances the influence of lithology on the spacing of fluid-driven joints. When bedding interfaces are bonded together, the driving stress distribution around a dilated, pressurized crack is not significantly affected by the thickness of adjacent, unfractured beds. Consequently, in the absence of interbed slip, fluid-driven joint spacing should not be strongly influenced by the thickness of adjacent, unfractured beds.

## Acknowledgments

This paper represents a portion of M.P. Fischer's Ph.D. dissertation at Penn State University. R.B. Alley, D. Fisher, and D. Elsworth are acknowledged for their comments on Fischer's dissertation. We thank T. Ingraffea for allowing us to use FRANC, and acknowledge the technical assistance of P. Wawrzynek, D. Swenson and T. Bittencourt during our use of the program. Computational facilities for this study were provided by R.B. Alley. We gratefully acknowledge support of the David and Lucile Packard Foundation and grants NSF DPP-8822027 and DPP-8915995

in the acquisition and maintenance of these facilities. E.H. Rutter and one anonymous reviewer are acknowledged for their comments and suggestions on this manuscript.

## References

- Achenbach, J.D., Keer, L.M., Khetan, R.P. and Chen, S.H., 1979. Loss of adhesion at the tip of an interface crack. *J. Elasticity*, 9: 397–424.
- Apotria, T., Kaiser, C.J. and Cain, B.A., 1994. Fracturing and stress history of the Devonian Antrim Shale, Michigan basin. In: P.P. Nelson and S.E. Laubach (Editors), *Rock Mechanics: Models and Measurements, Challenges from Industry*. Proc. First Conference of the North American Rock Mechanics Society, A.A. Balkema, Rotterdam, pp. 809–816.
- Atkinson, B.K. and Meredith, P.G., 1987a. The theory of subcritical crack growth with applications to minerals and rocks. In: B.K. Atkinson (Editor), *Fracture Mechanics of Rock*. Academic Press, London, England, pp. 111–166.
- Atkinson, B.K. and Meredith, P.G., 1987b. Experimental fracture mechanics data for rocks and minerals. In: B.K. Atkinson (Editor), *Fracture Mechanics of Rock*. Academic Press, London, England, pp. 477–525.
- Barsoum, R.S., 1976. On the use of isoparametric finite elements in linear fracture mechanics. *Int. J. Num. Meth. Eng.*, 10: 25–37.
- Bell, J.S., 1990. The stress regime of the Scotian Shelf offshore eastern Canada to 9 kilometers depth and implications for rock mechanics and hydrocarbon migration. In: V. Maury and D. Fourmaintraux (Editors), *Rock at Great Depth*. Balkema, Rotterdam, pp. 1243–1265.
- Birch, F., 1966. Compressibility; elastic constants. In: S.P. Clark Jr., (Editor), *Handbook of Physical Constants*. Geol. Soc. Am. Mem., 97: 97–173.
- Bittencourt, T.N., Barry, A. and Ingraffea, A.R., 1992. Comparison of mixed-mode stress intensity factors obtained through displacement correlation, J-integral formulation, and modified crack-closure integral. In: S.N. Atluri, J.C. Newman Jr., I.S. Raju and J.S. Epstein (Editors), *Fracture Mechanics: 22nd Symposium*. Am. Soc. Testing Materials, Spec. Tech. Publ., 1131(2): 69–82.
- Blair, B.E., 1955. Physical properties of mine rock, Part 3. U.S. Bur. Mines, Rep. Invest. 5130, Washington, D.C., 69 pp.
- Blair, B.E., 1956. Physical properties of mine rock, Part 4. U.S. Bur. Mines, Rep. Invest. 5244, Washington, D.C., 69 pp.
- Breckels, I.M. and van Eekelen, H.A.M., 1982. Relationship between horizontal stress and depth in sedimentary basins. *J. Pet. Technol.*, 34: 2191–2199.
- Broek, D., 1986. *Elementary Engineering Fracture Mechanics*. Sijthoff and Noordhoff International Publishers, Alphen a/d Rijn, The Netherlands, 437 pp.
- Engelder, T., 1987. Joints and shear fractures in rock. In: B.K. Atkinson (Editor), *Fracture Mechanics of Rock*. Academic Press, London, England, pp. 27–69.
- Engelder, T. and Fischer, M.P., 1994. Influence of poroelastic behavior on the magnitude of minimum horizontal stress,  $S_h$ , in overpressured parts of sedimentary basins. *Geology*, 22: 949–952.
- Engelder, T. and Lacazette, A., 1990. Natural hydraulic fracturing. In: *Proceedings, International Symposium on Rock Joints*. Loen, Norway, pp. 35–43.
- Fischer, M.P., 1994. Application of linear elastic fracture mechanics to some problems of fracture propagation in rock and ice. Ph.D. Thesis, The Pennsylvania State Univ., University Park, PA, 232 pp. (unpubl.).
- Fischer, M.P. and Engelder, T., 1994. Heterogeneous hydrofracture development and accretionary fault dynamics: Comment. *Geology*, 22: 1052–1053.
- Gaarenstroom, L., Tromp, R.A.J., de Jong, M.C. and Brandenburg, A.M., 1993. Overpressures in the central North Sea: Implications for trap integrity and drilling safety. In: J.R. Parker (Editor), *Petroleum Geology of Northwestern Europe: Proceedings of the Fourth Conference*. Geol. Soc. London, pp. 1305–1313.
- Gross, M.R., 1993a. The origin and spacing of cross joints: examples from the Monterey Formation, Santa Barbara coastline, California. *J. Struct. Geol.*, 15: 737–751.
- Gross, M.R., 1993b. The influence of mechanical stratigraphy on deformation mode and joint spacing in the Monterey Formation. Ph.D. Thesis, The Pennsylvania State Univ., University Park, PA, 183 pp. (unpubl.).
- Gross, M.R., Fischer, M.P., Engelder, T. and Greenfield, R.J., in press. Factors controlling joint spacing in interbedded sedimentary rocks: Integrating numerical models with field observations. *J. Geol. Soc. London*.
- Harris, J.F., Taylor, G.L. and Walper, J.L., 1960. Relation of deformational fractures in sedimentary rocks to regional and local structures. *Am. Assoc. Pet. Geol. Bull.*, 44: 1853–1873.
- Hatheway, A.W. and Kiersch, G.A., 1982. Engineering properties of rock. In: R.S. Carmichael (Editor), *Handbook of Physical Properties Rock*, 1. CRC Press Inc., Boca Raton, FL, pp. 289–331.
- Helgeson, D.E. and Aydin, A., 1991. Characteristics of joint propagation across layer interfaces in sedimentary rocks. *J. Struct. Geol.*, 13: 987–911.
- Hobbs, D.W., 1967. The formation of tension joints in sedimentary rocks: An explanation. *Geol. Mag.*, 104: 550–556.
- Huang, Q. and Angelier, J., 1989. Fracture spacing and its relation to bed thickness. *Geol. Mag.*, 126: 355–362.
- Ingraffea, A.R., 1990. Case studies of simulation of fracture in concrete dams. *Eng. Fract. Mech.*, 35: 553–564.
- Keer, L.M. and Chen, S.H., 1981. The intersection of a pressurized crack with a joint. *J. Geophys. Res.*, 86: 1032–1038.
- Kümpel, H.-J., 1991. Poroelasticity: parameters reviewed. *Geophys. J. Int.*, 105: 783–799.
- Lachenbruch, A.H., 1961. Depth and spacing of tension cracks. *J. Geophys. Res.*, 66: 4273–4292.

- Ladeira, F.L. and Price, N.J. 1981. Relationship between fracture spacing and bed thickness. *J. Struct. Geol.*, 3: 179–183.
- Lawn, B.R. and Wilshaw, T.R., 1975. *Fracture of Brittle Solids*. Cambridge University Press, Cambridge, England, 204 pp.
- Linsbauer, H.N., Ingraffea, A.R., Rossmanith, H.P. and Wawrzynek, P.A., 1989. Simulation of cracking in large arch dam: Part II. *J. Struct. Eng.*, 115: 1616–1630.
- McQuillan, H. 1973. Small-scale fracture density in Asmari Formation of southwest Iran and its relation to bed thickness and structural setting. *Am. Assoc. Pet. Geol. Bull.*, 57: 2367–2385.
- Narr, W. and Suppe, J., 1991. Joint spacing in sedimentary rocks. *J. Struct. Geol.*, 13: 1037–1048.
- Olson, J.E., 1993. Joint pattern development: Effects of sub-critical crack growth and mechanical crack interaction. *J. Geophys. Res.*, 98: 12,251–12,265.
- Pollard, D.D. and Segall, P. 1987. Theoretical displacements and stresses near fracture in rock: with applications to faults, joints, veins, dikes, and solution surfaces. In: B.K. Atkinson (Editor), *Fracture Mechanics of Rock*. Academic Press, London, England, pp. 277–349.
- Price, N.J., 1966. *Fault and Joint Development in Brittle and Semi-Brittle Rocks*. Pergamon Press, Oxford, England, 176 pp.
- Rives, T., Razack, M., Petit, J.-P. and Rawnsley, K.D., 1992. Joint spacing: analogue and numerical simulations. *J. Struct. Geol.*, 14: 925–937.
- Rives, T., Rawnsley, K.D. and Petit, J.-P., 1994. Analogue simulation of natural orthogonal joint set formation in brittle varnish. *J. Struct. Geol.*, 16: 419–429.
- Salz, L.B., 1977. Relationship between fracture propagation pressure and pore pressure. Paper 6870, presented at the Annu. Meeting Soc. Pet. Eng., Denver, CO, October 9–12.
- Secor, D.T., 1965. Role of fluid pressure in jointing. *Am. J. Sci.*, 263: 633–646.
- Senseney, P.E. and Pfeifle, T.W., 1984. Fracture toughness of sandstones and shales. In: *Rock Mechanics in Productivity and Protection*. Proc. 25th U.S. Symposium on Rock Mechanics, Soc. Min. Eng. Am. Inst. Min., Metall. Pet. Eng. Inc., New York, NY, pp. 390–397.
- Teufel, L.W., Rhett, D.W. and Farrell, H.E., 1991. Effect of reservoir depletion and pore pressure drawdown on in situ stress and deformation in the Ekofisk Field, North Sea. Proc. 32nd U.S. Rock Mechanics Symposium, pp. 63–72.
- Watkins, T.R., 1992. The fracture behavior of silicon carbide-graphite composites. Ph.D. Thesis, The Pennsylvania State University, University Park, PA, 287 pp. (unpubl).
- Wawrzynek, P.A. and Ingraffea, A.R., 1987. Interactive finite element analysis of fracture processes: An integrated approach. *Theor. Appl. Frac. Mech.*, 8: 137–150.